Radiolabeled Small-Molecule Ligands for Prostate-Specific Membrane Antigen: *In vivo* Imaging in Experimental Models of Prostate Cancer

Catherine A. Foss,[1] Ronnie C. Mease,[1] Hong Fan,[1] Yuchuan Wang,[1] Hayden T. Ravert,[1] Robert F. Dannals,[1] Rafal T. Olszewski,[2] Warren D. Heston,[3] Alan P. Kozikowski,[4] and Martin G. Pomper[1]

Abstract

Purpose: Prostate-specific membrane antigen (PSMA) is a cell surface protein that is overexpressed in prostate cancer, including hormone-refractory and metastatic disease. Our goal in this study was to develop a series of PSMA-based imaging agents for clinical use.

Experimental Design: We have synthesized and evaluated the *in vivo* biodistribution of two radiolabeled urea derivatives that have high affinity for PSMA in severe combined immunodeficient mice harboring MCF-7 (breast, PSMA-negative), PC-3 (prostate, PSMA-negative), and LNCaP (prostate, PSMA-positive) xenografts. Radiopharmaceutical binding selectivity and tumor uptake were also evaluated *in vivo* using dedicated small animal positron emission tomography, single photon emission computed tomography, and gamma scintigraphic imaging devices. *N*-[*N*-[(*S*)-1,3-dicarboxypropyl]carbamoyl]-*S*-[^{11}C]methyl-L-cysteine ([^{11}C]DCMC K_i, 3.1 nmol/L) and *N*-[*N*-[(*S*)-1,3-dicarboxypropyl]carbamoyl]-*S*-3-[^{125}I]iodo-L-tyrosine ([^{125}C]DCIT K_i, 1.5 nmol/L) were synthesized using [^{11}C]CH_3I and with [^{125}I]NaI/Iodogen, respectively.

Results: At 30 minutes postinjection, [^{11}C]DCMC and [^{125}I]DCIT showed tumor/muscle ratios of 10.8 and 4.7, respectively, with clear delineation of LNCaP-derived tumors on imaging. MCF-7- and PC-3-derived tumors showed significantly less uptake of [^{11}C]DCMC or [^{125}I]DCIT.

Conclusion: These results show the feasibility of imaging PSMA-positive prostate cancer using low molecular weight agents.

Prostate cancer will be diagnosed and treated in 230,000 men in the United States in 2004 (1). Prostate cancer is currently diagnosed by sector biopsy in men presenting with an elevated serum prostate-specific antigen level. As for all biopsies, sector biopsy for prostate cancer is invasive and limited by sampling error. More accurate staging would facilitate treatment decisions and lead to a better outcome for patients. Badly needed is a method by which to detect small lesions (i.e., recurrent tumors in the surgical bed) and other subtle manifestations of the disease in men with an elevated serum prostate-specific antigen but no other symptoms. Diagnostic imaging could provide a full picture of prostate tumor burden by uncovering recurrent and metastatic lesions. Particularly useful would be an imaging technique that could be correlated with a relevant tumor phenotype (e.g., serve as a biomarker for androgen-independent disease).

Prostate-specific membrane antigen (PSMA) provides an excellent target for prostate tumor imaging and therapy because of its transmembrane location and the fact that it is significantly up-regulated in prostate cancer and metastasis relative to the few normal tissues in which it resides (2). PSMA is also strongly expressed in the neovasculature of many solid tumors but oddly enough not in that of prostate cancer (3–5). ^{111}In-Capromab pendetide (ProstaScint) is a commercially available monoclonal antibody in clinical use for detecting prostate cancer but has been cited for complexities associated with its administration and the interpretation of the images obtained (6–8). Furthermore, antibody-mediated imaging is known to suffer from inherently difficult pharmacokinetics, including limited access to tumors and slow washout rates that produce significant background radioactivity (i.e., low signal-to-noise ratio; refs. 9, 10). We have synthesized two small-molecule ligands for PSMA, one in positron-emitting form (^{11}C) for positron emission tomography (PET) and the other labeled with ^{125}I for single photon emission computed tomography (SPECT) and gamma scintigraphy in rodents, and use them to perform imaging of PSMA-positive and PSMA-negative lesions in experimental models of prostate cancer *in vivo*.

Authors' Affiliations: [1]Johns Hopkins University, Baltimore, Maryland; [2]Georgetown University, Washington, District of Columbia; [3]The Cleveland Clinic Foundation, Cleveland, Ohio; and [4]University of Illinois at Chicago, Chicago, Illinois
Received 12/30/04; revised 3/1/05; accepted 3/14/05.

Grant support: NIH grants CA92871 (M.G. Pomper), CA101069 (W.D. Heston), and CA103175 (Zaver Bhujwalla, Johns Hopkins University).

The costs of publication of this article were defrayed in part by the payment of page charges. This article must therefore be hereby marked *advertisement* in accordance with 18 U.S.C. Section 1734 solely to indicate this fact.

Requests for reprints: Martin G. Pomper, Department of Radiology, Johns Hopkins University, 600 North Wolfe Street, Phipps B-100, Baltimore, MD 21287-2182. Phone: 410-955-2789; Fax: 410-614-1213; E-mail: mpomper@jhmi.edu.

Materials and Methods

Cell lines and mouse models. MCF-7, PC-3, and LNCaP cell lines were obtained from the American Type Culture Collection (Rockville, MD), maintained in EMEM (Mediatech, Inc., Herndon, VA; MCF-7) and RPMI 1640 (PC-3 and LNCaP), and supplemented as described previously (11). All cells were grown to 80% to 90% confluence before trypsinization and formulation into an equal volume of HBSS (Sigma, St. Louis, MO) and Matrigel (Becton Dickinson, San Jose, CA) for implantation into mice.

All animal studies were carried out in full compliance with institutional guidelines related to the conduct of animal experiments. Male (for PC-3 and LNCaP) or female (for MCF-7) severe combined immunodeficient (SCID) mice (Charles River Laboratories, Wilmington, MA) were implanted s.c. with 1×10^6 to 5×10^6 cells in Matrigel forward of the left flank. SCID mice were derived on a CD17 background. Mice were imaged or used in biodistribution assays when the tumor xenografts reached 5 to 7 mm in diameter. Glutamate carboxypeptidase II (GCPII) knockout mice were provided by Dr. Warren D. Heston and generated as described previously (12).

Chemistry and radiochemistry. All chemicals and solvents were of American Chemical Society or high-performance liquid chromatography (HPLC) purity and were used as received. Dimethylformamide was purified by stirring overnight with barium oxide and distilled before use. [^{11}C]Methyl iodide was produced using a General Electric PETtrace MeI Microlab (Twinsburg, OH). The HPLC system consisted of two Waters (Milfad, MA) model 590EF pumps, two Rheodyne (Rohnheit Park, CA) model 7126 injectors, an in-line Waters model 441 UV detector (254 nm), and a single [^{125}I]NaI crystal flow radioactivity detector. All HPLC chromatograms were recorded by a Rainin Dynamax (Varian Inc., Palo Alto, CA) dual-channel control/interface module connected to a Macintosh computer running Dynamax version 1.4 program software. Radioactivity measurements were made using a Capintec (Ramsey, NJ) CRC-15R dose calibrator.

Radiosynthesis of N-[N-[(S)-1,3-dicarboxypropyl]carbamoyl]-S-[^{11}C]methyl-L-cysteine. The *N*-[*N*-[(*S*)-1,3-dicarboxypropyl]carbamoyl]-*S*-[^{11}C]methyl-L-cysteine ([^{11}C]DCMC) precursor (*N*-[*N*-[(*S*)-1,3-dicarboxypropyl]carbamoyl]-L-cysteine) was synthesized as reported previously (13). The radiosynthesis of [^{11}C]DCMC (known previously as [^{11}C]MCG) has been published (14).

Radiosynthesis of N-[N-[(S)-1,3-dicarboxypropyl]carbamoyl]-S-3-[^{125}I]iodo-L-tyrosine. The *N*-[*N*-[(*S*)-1,3-dicarboxypropyl]carbamoyl]-*S*-3-[^{125}I]iodo-L-tyrosine ([^{125}I]DCIT) precursor (*N*-[*N*-[(*S*)-1,3-dicarboxypropyl]carbamoyl]-L-tyrosine) was synthesized as described previously (15). Radio-iodination of DCIT followed the Iodogen method (16). Briefly, DCIT precursor (100 μg) was dissolved in 100 μL phosphate-buffered NaCl solution (pH 7.5). This solution was added to a 4 mL glass vial containing 100 μg coated Iodogen. [^{125}I]NaI (1-5 mCi; MP Biomedicals, Costa Mesa, CA) was then added to the vial and the reaction proceeded at ambient temperature for 15 minutes. The solution was then withdrawn and purified by preparative HPLC. A Phenomenex (Torrance, CA) C_{18} Luna 250 × 10 mm column was used with 20% MeCN in 0.1% trifluoroacetic acid flowing at 6 mL/min. Product elution was monitored by a radioactivity detector and UV absorbance was monitored concurrently at 254 nm. The product was collected and concentrated under vacuum. [^{125}I]DCIT identity and purity were verified by analytic HPLC coinjection with unradiolabeled standard provided by Dr. Alan P. Kozikowski. Analytic HPLC conditions included the use of a 5.6 × 150 mm Phenomenex C_{18} Luna column flowing at 2 mL/min using 20% MeCN in 0.1% trifluoroacetic acid. The final product was formulated in sterile, physiologic NaCl solution at 1 mCi/mL and was filtered through a 0.22 μm syringe filter before storage in a sterile dose vial. The radiotracer was stored at 4°C until use.

In vitro *binding assays.* Taking advantage of the *N*-acetylaspartylglutamate (NAAG) peptidase activity of PSMA, the relative affinities of DCMC and DCIT for PSMA were determined using a previously published NAAG peptidase assay (17). Briefly, NAAG peptidase activity was determined using membranes of Chinese hamster ovary cells stably transfected with rat GCPII, 4 μmol/L NAAG as a substrate, and a trace amount of [^{3}H]NAAG. Inhibitors at concentrations of 0.1, 0.3, 1, 3, 10, 30, 100, 300, and 1,000 nmol/L were tested. Product was separated using ion-exchange chromatography (AG-50W-X8 analytic grade cation-exchange resin). The amount of [^{3}H]glutamate as a product of NAAG hydrolysis was determined by scintillation spectrophotometry.

In vivo *biodistribution.* [^{11}C]DCMC: Xenograft-bearing mice (17-20 g) were injected via the tail vein with 740 kBq (200 μCi, 6.49 pmol) [^{11}C]DCMC in 200 μL NaCl solution or were coinjected with [^{11}C]DCMC mixed with 50 mg/kg 2-(phosphonomethyl)pentanedioic acid (PMPA), a high-affinity inhibitor of PSMA (18), to effect PSMA blockade. Blood was collected immediately after sacrifice (cervical dislocation) by cardiac puncture and selected tissues were harvested, weighed, and counted in an automated gamma counter (LKB Wallac 1282 Compugamma CS Universal Gamma Counter, Perkin-Elmer, Boston, MA). Tissue radiopharmaceutical uptake values were calculated as percent injected dose per gram (%ID/g) compared with a 1:10 diluted standard dose. [^{125}I]DCIT: Male CD-1 mice (25-30 g) and xenograft-bearing severe combined immunodeficient mice (17-20 g) were injected via the tail vein with either 74 kBq (2 μCi, 1 pmol) [^{125}I]DCIT in 200 μL NaCl solution or 2 μCi [^{125}I]DCIT and 50 mg/kg PMPA blocker (Alexis Biochemicals, San Diego, CA) in 200 μL NaCl solution. Mice were sacrificed at 30, 60, and 90 minutes postinjection, tissues were harvested and counted, and results are presented as for [^{11}C]DCMC.

In vivo *imaging.* PET: Static images were acquired on an (Advanced Technology Laboratory Animal Scanner, NIH, Bethesda, MD) small animal PET scanner, which has a 2 cm axial field of view, depth-of-interaction capability, and an axial resolution of ~1.5 mm using an ordered subset expectation maximum (OSEM) reconstruction algorithm (19–22). Mice were injected i.v. with either 750 kBq (200 μCi, 6.49 pmol) [^{11}C]DCMC alone or with a coinjection of radiotracer and 50 mg/kg PMPA blocker in 200 μL NaCl solution. Anesthesia was induced with a s.c. injection of ketamine/acepromazine cocktail before positioning the animal on the scanner and was maintained with isoflurane. A 10-minute static image of two mice side-by-side (one unblocked and one blocked) was acquired at 30 minutes after administration of the radiotracer via the tail vein. Images were reconstructed using the OSEM algorithm (22). SPECT and planar gamma scintigraphy: Mice were injected i.v. with either 5.55 MBq (150 μCi, 75 pmol) [^{125}I]DCIT in 200 μL NaCl solution or a coinjection of 5.55 MBq [^{125}I]DCIT and 50 mg/kg PMPA blocker in 200 μL NaCl solution. Mice were imaged at 30 minutes postinjection using a 10-minute static scan. Mice were anesthetized as for [^{11}C]DCMC. Static images were acquired on a X-SPECT small animal scanner (Gamma Medica, Inc., Northridge, CA) using either a single-head, high-resolution (1-3 mm) parallel hole or pinhole collimator.

Statistical analysis. StatView 5.0 (SAS Institute, Inc., Cary, NC) was used for statistical analysis. A paired *t* test was used to assess for differences in tumor radiopharmaceutical uptake between different tissues. *P*s < 0.01 were considered significant.

Results and Discussion

[^{11}C]DCMC and [^{125}I]DCIT are readily synthesized and show high affinity to PSMA. An important feature of any new radiopharmaceutical is the ability for it to be generated in radiolabeled form easily (i.e., introduction of the radiolabel in the last step of the synthesis, in high yield, and in high specific radioactivity). Both [^{11}C]DCMC and [^{125}I]DCIT fulfill all of those criteria, with [^{11}C]DCMC synthesized in 3 minutes by *S*-[^{11}C] methylation (14) and [^{125}I]DCIT by the standard

Iodogen method (23). [^{125}I]DCIT was produced routinely in specific radioactivities >54 MBq/μmol (2,000 Ci/mmol). The radiochemical yield was typically 80% and the radiochemical purity was >99%. [^{11}C]DCMC is a positron-emitting, PSMA-based imaging agent. Despite the short physical half-life of ^{11}C ($t_{1/2}$, 20 minutes), many useful PET imaging agents employ this radionuclide, which requires a cyclotron on-site. The strategy in synthesizing [^{125}I]DCIT was to model production of a radiopharmaceutical with a longer physical half-life than ^{11}C for clinical applications, such as ^{123}I ($t_{1/2}$, 13 hours) for SPECT or ^{124}I ($t_{1/2}$, 4.2 days) for PET. ^{125}I was chosen for these studies because of its low cost, its ready availability, and its ability to be imaged in animal models of human cancer easily using a dedicated small animal device. Synthesis of the urea-based precursors to these compounds, which can provide access to a wide variety of structural analogs, is very straightforward, proceeding in only a few steps from the corresponding amino acids (13).

The affinities of DCMC, DCIT, and their precursors were measured in a GCPII-based assay (17). It is the NAAG peptidase (NAALADase) activity of GCPII that confers the PSMA-binding characteristics to these compounds because PSMA and NAALADase are the same enzyme (24, 25). DCMC and DCIT are not substrates for PSMA but are believed to bind electrostatically to the active site (26) so that PSMA is essentially behaving as a receptor for these ligands. The K_i values of DCMC and DCIT are 1.9 and 1.5 nmol/L, respectively, well within the range necessary for successful receptor-based radiopharmaceuticals (27).

[^{11}C]DCMC and [^{125}I]DCIT show specific binding to PSMA–containing tissue. A subset of proximal renal tubules contains the highest concentration of the carboxypeptidase activity of PSMA (i.e., GCPII) in humans and rodents (28, 29). The kidney is therefore the target organ and provides an initial screen for agents likely to bind to PSMA-positive prostate cancer. Mouse prostate does not contain appreciable levels of PSMA (14, 30). We used two different imaging methods to show PSMA-based binding of [^{11}C]DCMC and [^{125}I]DCIT. First, we imaged [^{11}C]DCMC and [^{125}I]DCIT with PET and planar gamma scintigraphy, respectively, both in the absence and in the presence of an excess of PMPA, which serves to block PSMA for binding of the imaging agents. Binding of [^{11}C]DCMC to kidneys (Fig. 1A) is selective, noted by decreased radioactivity within kidneys on the blocked images (Fig. 1B). That finding was in support of our earlier work demonstrating specific binding in an *ex vivo* biodistribution assay (14). Figure 2 shows similar blockade and therefore PSMA-specific binding for [^{125}I]DCIT. The second method to determine PSMA-binding selectivity included performing SPECT imaging of [^{125}I]DCIT in GCPII knockout mice (12). Figure 3A shows that renal activity is essentially absent in the knockout mouse after administration of [^{125}I]DCIT, indicating further that the high renal uptake noted in the *ex vivo* biodistribution assay (Table 1) is actually PSMA-mediated binding rather than being due merely to renal clearance. A preliminary *ex vivo* study in which GCPII−/−, GCPII+/−, and wild-type animals were given [^{125}I]DCIT showed incremental increases in renal radiopharmaceutical binding at 30 minutes (15.43%, 176.14%, and 241.13% ID/g, n = 1 animal each, respectively). Heterozygous animals are known to possess intermediate levels of GCPII. A full *ex vivo* biodistribution assay for [^{11}C]DCMC in CD-1 mice has been published (14).

[^{11}C]DCMC and [^{125}I]DCIT show specific binding to PSMA–positive prostate tumor xenografts. The LNCaP line of human prostate cancer is a model often used to investigate PSMA-based imaging and therapeutic approaches (31–33). The only clinically approved prostate cancer–specific imaging agent, ProstaScint, involves a radioimmunodiagnostic method that made much use of LNCaP-derived xenografts during preclinical development to show binding specificity (32). Other, potentially clinically superior, PSMA-based radioantibodies have also been evaluated initially in LNCaP-derived tumors (34). We used LNCaP-derived xenografts as a model for PSMA-positive tumors and PC-3 (prostate cancer) and MCF-7 (breast cancer) xenografts as PSMA-negative controls. Table 2 shows the tumor/muscle and tumor/blood ratios for LNCaP-derived tumors, which were 10.78 and 8.31 for [^{11}C]DCMC and 4.69 and 1.52 for [^{125}I]DCIT, respectively. For [^{11}C]DCMC, those ratios were significantly different with Ps of 0.0003 and 0.0002, respectively. Differences in uptake of [^{11}C]DCMC between LNCaP and MCF-7 and PC-3 tumors

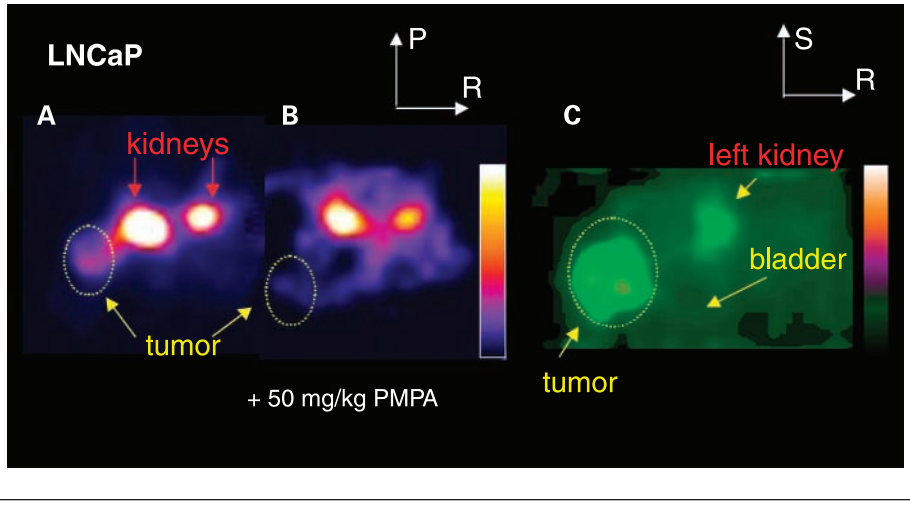

Fig. 1. *A,* axial advanced technology laboratory animal scanner PET images of [^{11}C]DCMC in mouse kidney and LNCaP tumors without and with (*B*) coinjection of 50 mg/kg PMPA to block PSMA. Note the decrease in tumor as well as renal radiopharmaceutical uptake on blockade in (*B*). *C,* magnified, coronal reconstructed image of animal in (*A*) outside of the plane of the kidneys immediately after urination indicates lack of specific binding to bladder. Tumor was clearly visualized as well as a portion of the left kidney. Images (*A* and *B*) are scaled to the same maximum. *P,* posterior; *R,* right; *S,* superior.

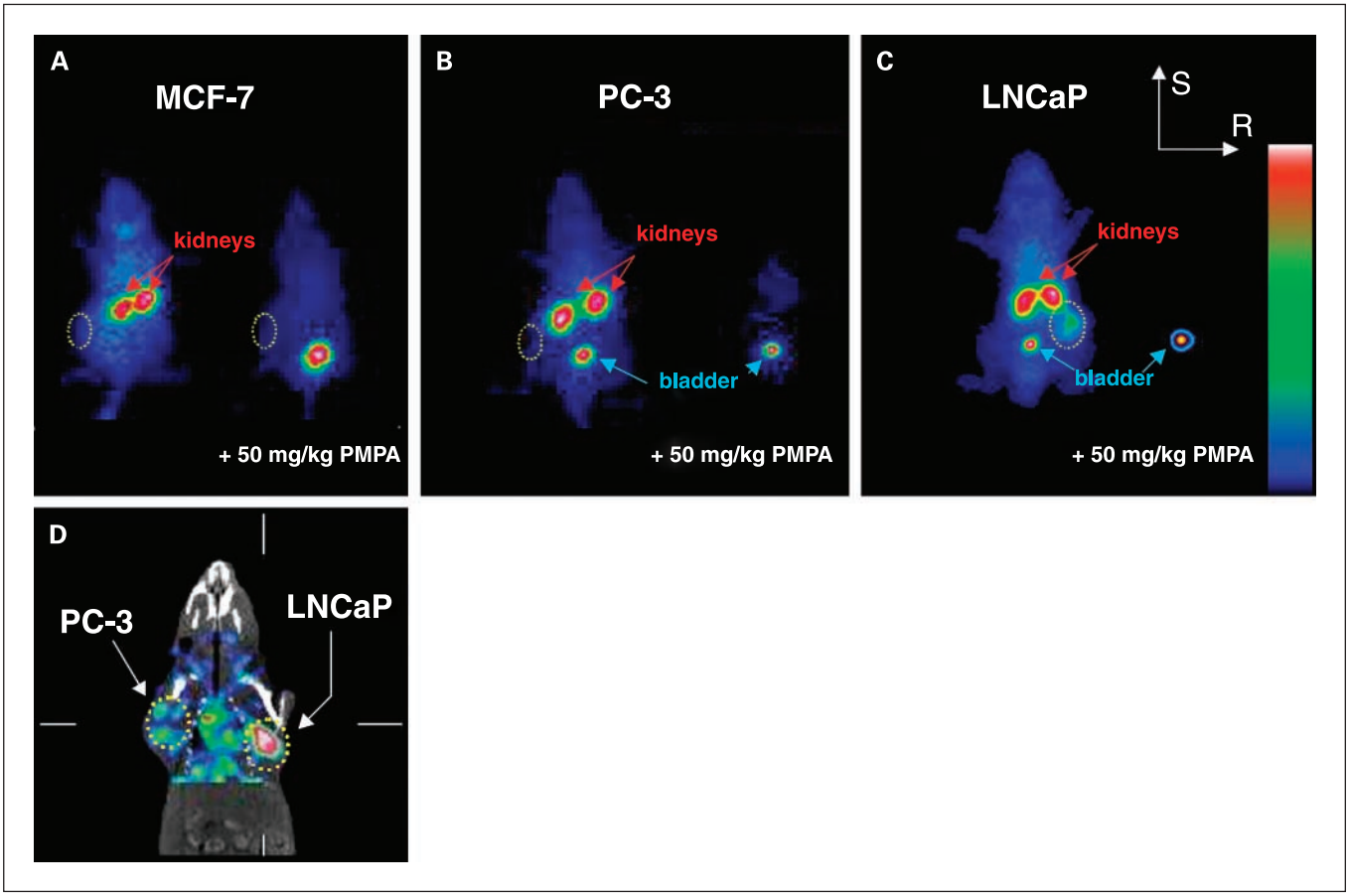

Fig. 2. Planar gamma scintigraphy of [^{125}I]DCIT in mouse kidney and tumors without (*left mouse*) and with (*right mouse*) coinjection of 50 mg/kg PMPA. Tumor is within dashed circles. Again, note decreased radiopharmaceutical uptake within kidneys on blockade. Only the LNCaP tumor was visualized (*C*). SPECT with computed tomography overlay (*D*) further shows the LNCaP tumor, whereas the PC-3 tumor retains only minimal radiotracer. Images (*A*-*C*) are scaled to the same maximum (bladder or kidney).

were also significant, both with $P = 0.0001$. For PSMA blockade, the decrease in [^{11}C]DCMC for LNCaP tumors seen on blockade was significant ($P = 0.0015$). Differences between tumor and blood or muscle [^{11}C]DCMC uptake for MCF-7 and PC-3 tumors were not significant. For [^{125}I]DCIT, differential uptake between tumor and muscle was significant ($P = 0.01$), as was the difference between unblocked and blocked LNCaP tumors ($P = 0.01$). Differences in tumor/

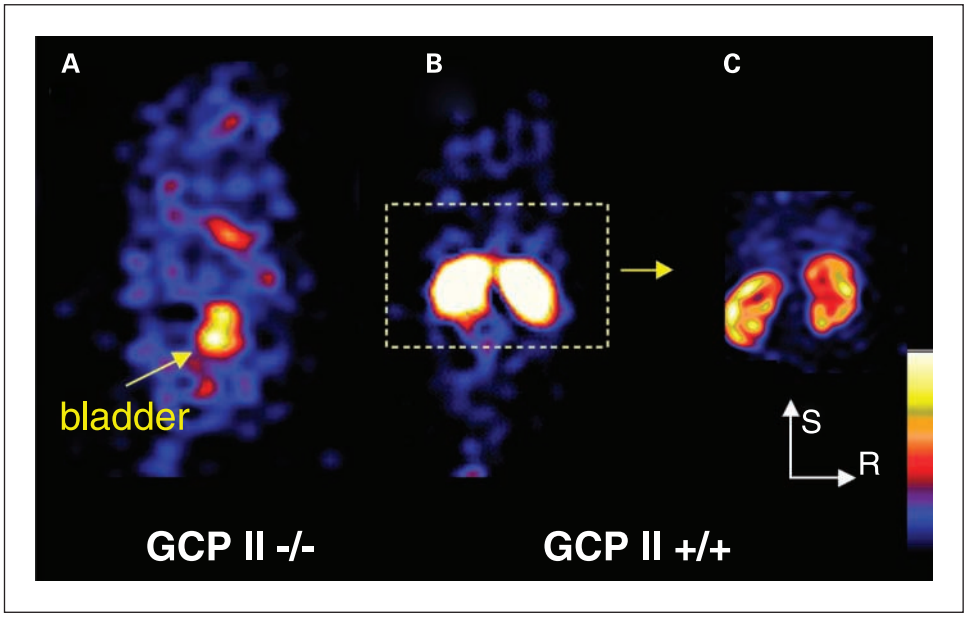

Fig. 3. SPECT imaging of [^{125}I]DCIT in GCPII knockout (*A*) and wild-type (*B* and *C*) animals. Images (*A* and *B*) were obtained with a parallel-hole collimator and are scaled to the same maximum. Image (*C*) is from the same animal as in (*B*), except using a higher-resolution, pinhole collimator. Animals devoid of GCPII show no renal binding of radiopharmaceutical.

Table 1. Biodistribution of [^{125}I]DCIT in CD-1 mice (%ID/g; $n = 4$)

Tissue	30 min	60 min	90 min
Blood	4.64 ± 3.21	1.54 ± 0.26	2.92 ± 1.29
Urinary bladder	4.28 ± 3.04	2.02 ± 0.97	1.63 ± 0.48
Muscle	0.82 ± 0.47	1.14 ± 0.83	1.27 ± 0.57
Kidneys	62.21 ± 10.78	18.22 ± 6.56	7.20 ± 0.93
Kidney/muscle	75.85	15.98	5.67
Kidney/blood	13.4	11.83	2.47

muscle for [^{125}I]DCIT were not significant for the MCF-7 or PC-3 tumors. The relatively higher tumor/background ratios for [^{11}C]DCMC compared with [^{125}I]DCIT may reflect the lower lipophilicity of the former [CLog $P = -0.06$, versus 1.11 by KowWin (http://www.syrres.com)]. Notably, the criteria for ProstaScint to progress to the clinic required a 3:1 tumor/muscle (background) ratio in s.c. LNCaP tumors, and a similar uptake ratio shown in the clinic provided a positive predictive value for the presence of prostate cancer at >90% (29). Nevertheless, ProstaScint is the current clinical standard and any potential new prostate cancer imaging agent must prove superior or at least complementary to it.

Imaging studies employing PET and planar gamma scintigraphy corroborated highest PSMA-based binding of [^{11}C]DCMC and [^{125}I]DCIT to PSMA-positive tumors (Figs. 1, 2, and 4). Coinjection of the animals with PMPA showed blockade of radiopharmaceutical uptake in LNCaP-derived xenografts (Fig. 1B). Despite the lower LNCaP tumor uptake of [^{125}I]DCIT, clear images of the tumor could be delineated (Fig. 2C and D).

Implications for human prostate cancer diagnosis and therapy. As suggested at the outset, prostate cancer is the leading cancer in men and the second most common cause of cancer-related death. Furthermore, by the time of diagnosis, only half of the tumors are clinically localized and half of those represent extracapsular spread (35). Sensitive, functional imaging techniques are needed to (*a*) identify the extent of disease (metastases) in local lymph nodes before therapy, (*b*) identify the site of recurrence in patients with increasing serum prostate-specific antigen after surgery, and (*c*) study the surgical/radiotherapy bed without the confounds of blood pooling and other prohibitive pharmacokinetic phenomena that are characteristic of currently available agents. We believe that our small-molecule agents will possess the necessary characteristics to meet those challenges.

We emphasize that these are low molecular weight imaging agents (~300 g/mol) because of the potentially salutary pharmacokinetics of such agents for tumor imaging. Blood-borne molecules, whether therapeutic or diagnostic agents, must reach the tumor vasculature, cross the vessel wall to the interstitium, and then migrate through the interstitium to the target sites, which may be intracellular (9). There are microvascular barriers to the delivery of agents to tumors, which have a high interstitial fluid pressure due to collagen content and structure and high vascular permeability. The average uptake of agents to tumors actually decreases as the tumor increases in size (36). We believe that our small-molecule agents will gain access to their target sites more easily than antibody (i.e., ProstaScint) or polymeric agents (37).

Our agents bind to the extracellular active site of PSMA. That may be another advantage over ProstaScint, which binds to an internal epitope of PSMA, suggesting that cells must be dead or dying for ProstaScint to gain access to the target (6, 7). Arguably, the dead and dying cells will not represent the most aggressive elements of the tumor and would be less relevant targets for imaging. Prostate tumors tend to be small and vital, with little necrosis (38). Because of the heterogeneous tumor vasculature, an antibody-mediated agent may not gain access to all portions of the tumor, whereas a small molecule might. The large size of antibodies tends to increase their serum half-life so that there is slow diffusion from the tumor vasculature (39). Such prolonged clearance kinetics and slow tumor uptake provide low radiolocalization indices and high background radioactivity. Those findings have been the basis of the development of minibodies and diabodies (i.e., strategies to preserve the targeting specificity inherent to antibodies while decreasing their molecular weight to improve pharmacokinetics for imaging and therapy).

In addition to the benefits discussed above for imaging prostate cancer, PSMA is present in the neovasculature of a variety of tumors, including non–small cell lung cancer, colorectal carcinoma, and glioblastoma, suggesting that our agents may enable imaging of a wide variety of tumors. That has further implications for therapeutic monitoring of antiangiogenesis or antivascular therapies. We may also be

Table 2. Biodistribution of [^{11}C]DCMC and [^{125}I]DCIT in tumor-bearing mice (%ID/g; $n = 4$) at 30 minutes postinjection

[^{11}C]DCMC Tissue	MCF-7	PC-3	LNCaP
Tumor	0.32 ± 0.12	1.65 ± 0.29	8.73 ± 0.73
Muscle	0.25 ± 0.08	0.79 ± 0.47	0.81 ± 0.20
Blood	0.68 ± 0.18	2.12 ± 0.83	1.05 ± 0.07
Small intestine	0.40 ± 0.13	0.96 ± 0.04	0.89 ± 0.57
Tumor/muscle	1.28	2.10	10.78
Tumor/blood	0.47	0.78	8.31
Tumor + PMPA*	0.33 ± 0.24	1.74 ± 0.37	0.85 ± 0.37†
[^{125}I]DCIT Tissue	**MCF-7†**	**PC-3**	**LNCaP**
Tumor	2.43 ± 0.59	1.78 ± 0.63	5.07 ± 1.02
Muscle	0.85 ± 0.11	0.88 ± 0.18	1.08 ± 0.53
Blood	4.48 ± 0.36	2.60 ± 0.13	3.33 ± 1.36
Small intestine	1.03 ± 0.30	1.01 ± 0.03	1.79 ± 0.56
Tumor/muscle	2.86	2.02	4.69
Tumor/blood	0.54	0.68	1.52
Tumor + PMPA*	2.37 ± 1.44	3.97 ± 1.78	1.87 ± 0.45†

* PMPA was given as a 50 mg/kg coinjection.
† n = 3.

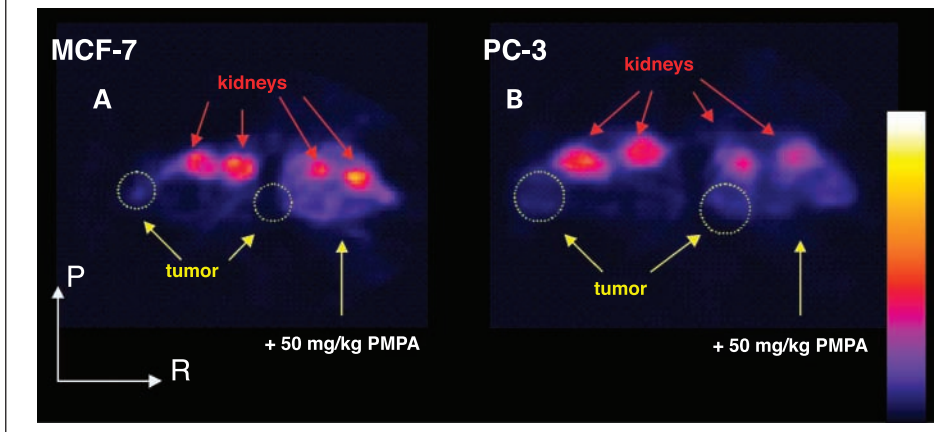

Fig. 4. Axial advanced technology laboratory animal scanner PET images of [^{11}C]DCMC in (*A*) MCF-7 and (*B*) PC-3 tumor-bearing mice. Pre-blockade images (left mouse) and those with coinjection of 50 mg/kg PMPA blocker (right mouse). PMPA decreased uptake within renal cortex (site of proximal tubules, replete with PSMA), but neither of these PSMA-negative tumors could be imaged clearly with this agent.

able to perform therapeutic monitoring of hormone-based therapies for prostate cancer because PSMA expression is sensitive to (inversely related to) steroid hormone levels (40). Accordingly, our agents may complement another recently reported small-molecule prostate cancer–specific agent, [^{18}F]fluorodihydrotestosterone (41), which binds to androgen receptor–positive tumors. For these reasons, we believe that we have the rudiments of a novel and practical approach to prostate cancer imaging.

Acknowledgments

We thank Dr. Barbara Wroblewska for helping to execute the NAAG peptidase assay and Kelley Harsch and James Fox for excellent technical assistance.

References

1. Leach F. Targeting prostate-specific membrane antigen in cancer therapy: can molecular medicine be brought to the surface? Cancer Biol Ther 2004;3:559–60.
2. Ghosh A, Heston WD. Tumor target prostate specific membrane antigen (PSMA) and its regulation in prostate cancer. J Cell Biochem 2004;91:528–39.
3. Chang SS, O'Keefe DS, Bacich DJ, Reuter VE, Heston WD, Gaudin PB. Prostate-specific membrane antigen is produced in tumor-associated neovasculature. Clin Cancer Res 1999;5:2674–81.
4. Chang SS, Reuter VE, Heston WD, Bander NH, Grauer LS, Gaudin PB. Five different anti-prostate-specific membrane antigen (PSMA) antibodies confirm PSMA expression in tumor-associated neovasculature. Cancer Res 1999;59:3192–8.
5. Chang SS. Monoclonal antibodies and prostate-specific membrane antigen. Curr Opin Investig Drugs 2004;5:611–5.
6. Milowsky MI, Nanus DM, Kostakoglu L, Vallabhajosula S, Goldsmith SJ, Bander NH. Phase I trial of yttrium-90-labeled anti-prostate-specific membrane antigen monoclonal antibody J591 for androgen-independent prostate cancer. J Clin Oncol 2004;22:2522–31.
7. Troyer JK, Beckett ML, Wright GL Jr. Location of prostate-specific membrane antigen in the LNCaP prostate carcinoma cell line. Prostate 1997;30:232–42.
8. Ponsky LE, Cherullo EE, Starkey R, Nelson D, Neumann D, Zippe CD. Evaluation of preoperative ProstaScint scans in the prediction of nodal disease. Prostate Cancer Prostatic Dis 2002;5:132–5.
9. Jain RK. Transport of molecules, particles, and cells in solid tumors. Annu Rev Biomed Eng 1999;1:241–63.
10. Sundaresan G, Yazaki PJ, Shively JE, et al. ^{124}I-labeled engineered anti-CEA minibodies and diabodies allow high-contrast, antigen-specific small-animal PET imaging of xenografts in athymic mice. J Nucl Med 2003;44:1962–9.
11. Soule HD, Vazguez J, Long A, Albert S, Brennan M. A human cell line from a pleural effusion derived from a breast carcinoma. J Natl Cancer Inst 1973;51:1409–16.
12. Bacich DJ, Ramadan E, O'Keefe DS, et al. Deletion of the glutamate carboxypeptidase II gene in mice reveals a second enzyme activity that hydrolyzes *N*-acetylaspartylglutamate. J Neurochem 2002;83:20–9.
13. Kozikowski AP, Nan F, Conti P, et al. Design of remarkably simple, yet potent urea-based inhibitors of glutamate carboxypeptidase II (NAALADase). J Med Chem 2001;44:298–301.
14. Pomper MG, Musachio JL, Zhang J, et al. ^{11}C-MCG: synthesis, uptake selectivity, and primate PET of a probe for glutamate carboxypeptidase II (NAALADase). Mol Imaging 2002;1:96–101.
15. Kozikowski AP, Zhang J, Nan F, et al. Synthesis of urea-based inhibitors as active site probes of glutamate carboxypeptidase II: efficacy as analgesic agents. J Med Chem 2004;47:1729–38.
16. Fraker PJ, Speck JC Jr. Protein and cell membrane iodinations with a sparingly soluble chloroamide, 1,3,4,6-tetrachloro-3a,6a-diphrenylglycoluril. Biochem Biophys Res Commun 1978;80:849–57.
17. Fuhrman S, Palkovits M, Cassidy M, Neale JH. The regional distribution of *N*-acetylaspartylglutamate (NAAG) and peptidase activity against NAAG in the rat nervous system. J Neurochem 1994;62:275–81.
18. Jackson PF, Cole DC, Slusher BS, et al. Design, synthesis, and biological activity of a potent inhibitor of the neuropeptidase *N*-acetylated α-linked acidic dipeptidase. J Med Chem 1996;39:619–22.
19. Seidel J, Vaquero JJ, Green MV. Resolution uniformity and sensitivity of the NIH ATLAS small animal PET scanner: comparison to simulated LSO scanners without depth-of-interaction capability. IEEE Nucl Sci Symp Conf Rec 2001:1555–8.
20. Lee JS, Hagemann RL, Wang Y, Tsui BMW, Pomper MG. Performance evaluation of the NIH ATLAS small animal PET system. Society of Molecular Imaging; San Francisco, CA; 2003.
21. Shimoji K, Ravasi L, Schmidt K, et al. Measurement of cerebral glucose metabolic rates in the anesthetized rat by dynamic scanning with ^{18}F-FDG, the ATLAS small animal PET scanner, and arterial blood sampling. J Nucl Med 2004;45:665–72.
22. Yao R, Seidel J, Johnson CA, Daube-Witherspoon ME, Green MV, Carson RE. Performance characteristics of the 3-D OSEM algorithm in the reconstruction of small animal PET images. Ordered-subsets expectation-maximixation. IEEE Trans Med Imaging 2000;19:798–804.
23. Zalutsky MR, Narula AS. A method for the radiohalogenation of proteins resulting in decreased thyroid uptake of radioiodine. Int J Rad Appl Instrum [A] 1987;38:1051–5.
24. Carter RE, Feldman AR, Coyle JT. Prostate-specific membrane antigen is a hydrolase with substrate and pharmacologic characteristics of a neuropeptidase. Proc Natl Acad Sci U S A 1996;93:749–53.
25. O'Keefe DS, Heston WD. Clearing up the confusion over the glutamate carboxypeptidase II gene. Am J Med Genet 2004;130A:327; author reply 329–30.
26. Rong SB, Zhang J, Neale JH, Wroblewski JT, Wang S, Kozikowski AP. Molecular modeling of the interactions of glutamate carboxypeptidase II with its potent NAAG-based inhibitors. J Med Chem 2002;45:4140–52.
27. Eckelman WC, Reba RC, Gibson RE, et al. Receptor-binding radiotracers: a class of potential radiopharmaceuticals. J Nucl Med 1979;20:350–7.
28. Slusher BS, Tsai G, Yoo G, Coyle JT. Immunocytochemical localization of the *N*-acetyl-aspartyl-glutamate (NAAG) hydrolyzing enzyme *N*-acetylated α-linked acidic dipeptidase (NAALADase). J Comp Neurol 1992;315:217–29.
29. Tasch J, Gong M, Sadelain M, Heston WD. A unique folate hydrolase, prostate-specific membrane antigen (PSMA): a target for immunotherapy? Crit Rev Immunol 2001;21:249–61.
30. Tiffany CW, Lapidus RG, Merion A, Calvin DC, Slusher BS. Characterization of the enzymatic activity of PSM: comparison with brain NAALADase. Prostate 1999;39:28–35.
31. Israeli RS, Powell CT, Corr JG, Fair WR, Heston WD.

Expression of the prostate-specific membrane antigen. Cancer Res 1994;54:1807–11.

32. Barren RJ III, Holmes EH, Boynton AL, Misrock SL, Murphy GP. Monoclonal antibody 7E11.C5 staining of viable LNCaP cells. Prostate 1997;30:65–8.

33. Li Y, Tian Z, Rizvi SM, Bander NH, Allen BJ. *In vitro* and preclinical targeted α therapy of human prostate cancer with Bi-213 labeled J591 antibody against the prostate specific membrane antigen. Prostate Cancer Prostatic Dis 2002;5:36–46.

34. Vallabhajosula S, Smith-Jones PM, Navarro V, Goldsmith SJ, Bander NH. Radioimmunotherapy of prostate cancer in human xenografts using monoclonal antibodies specific to prostate specific membrane antigen (PSMA): studies in nude mice. Prostate 2004;58:145–55.

35. Kotzerke J, Gschwend JE, Neumaier B. PET for prostate cancer imaging: still a quandary or the ultimate solution? J Nucl Med 2002;43:200–2.

36. Jain RK. Delivery of molecular medicine to solid tumors: lessons from *in vivo* imaging of gene expression and function. J Control Release 2001;74:7–25.

37. Gao X, Cui Y, Levenson RM, Chung LW, Nie S. *In vivo* cancer targeting and imaging with semiconductor quantum dots. Nat Biotechnol 2004;22:969–76.

38. Lange PH. ProstaScint scan for staging prostate cancer. Urology 2001;57:402–6.

39. Jain M, Batra SK. Genetically engineered antibody fragments and PET imaging: a new era of radioimmunodiagnosis. J Nucl Med 2003;44:1970–2.

40. Chang SS, Gaudin PB, Reuter VE, O'Keefe DS, Bacich DJ, Heston WD. Prostate-specific membrane antigen: much more than a prostate cancer marker. Mol Urol 1999;3:313–20.

41. Larson SM, Morris M, Gunther I, et al. Tumor localization of 16β-^{18}F-fluoro-5α-dihydrotestosterone versus ^{18}F-FDG in patients with progressive, metastatic prostate cancer. J Nucl Med 2004;45:366–73.